

Autoignition-affected stabilization of laminar nonpremixed DME/air coflow flames

Sili Deng*, Peng Zhao, Michael E. Mueller, Chung K. Law

Department of Mechanical and Aerospace Engineering, Princeton University, Princeton, NJ 08544, USA

Abstract

The structure and stabilization mechanism of laminar nonpremixed autoignitive DME/air coflow flames were investigated under typical diesel engine conditions. The simulations were performed at 30 atmospheres with uniform inlet velocities of 3.2 m/s for both streams, and the coflow air boundary temperatures were 700, 800, 900, and 1100 K. The heat release rate and species profiles were examined for each case. Further investigation with Chemical Explosive Mode Analysis (CEMA) and Lagrangian Flamelet Analysis (LFA) were performed to identify the controlling chemistry and elucidate the dominant combustion mode and stabilization mechanism. At 700 to 900 K, autoignition was observed to be the dominant stabilization mechanism, and NTC chemistry determines the stabilization point in mixture fraction space. Moreover, the coupling between the autoignition process and premixed flame propagation results in multibrachial structure. Conversely, at 1100 K, the kinematic balance between premixed flame propagation velocity and the incoming flow velocity becomes the dominant stabilization mechanism, and the classical triple flame structure was observed. Extended stabilization regimes, in terms of increasing boundary temperature, are therefore identified, including frozen flow, purely kinetically stabilized, autoignition-propagation-coupled stabilized, purely kinematically stabilized, and burner stabilized regimes.

Keywords: Stabilization, Nonpremixed coflow flame, Autoignition, Negative Temperature Coefficient (NTC), Dimethyl ether (DME)

1. Introduction

Nonpremixed jet flames have been extensively studied to understand the combustion processes in diesel engines. The stabilization and structure of jet flames determine the lift-off height of the flame and is therefore crucial to engine design. Due to the mixing process of the fuel and oxidizer streams in lifted flames, the combustion mode is partially premixed, resulting in a two-dimensional tribrachial flame (also known as triple flame) [1], specifically, a lean and a rich premixed flame wing with a trailing diffusion flame branch. The point where the three branches intersect is called the triple point and is generally considered to be the stabilization point for nonautoignitive situations. The

*Corresponding Author: silideng@princeton.edu

dynamic balance between the local flame propagation speed and the incoming flow speed is characterized as the stabilization mechanism. A recent review by Chung [2] discussed the stabilization, propagation, and instability of tribrachial flames, including the effects of concentration gradient [3–5], velocity gradient [6], and burned gas expansion [7–10]. These studies, however, were limited to nonautoignitive conditions, but real diesel engines are operated at elevated pressures and temperatures, where autoignition is activated and could interact with the tribrachial flame.

Chung and co-workers [11–13] conducted a series of experiments to investigate the autoignition characteristics of laminar C_1 to C_4 fuel jets in a heated air coflow and found that, above certain coflow temperatures, lifted flames could be established through autoignition. In these studies, both the tribrachial structure for most autoignited cases and a repetitive behavior of extinction and reignition at the critical condition near blowout were observed. However, the role that autoignition plays in the stabilization mechanism as well as its influences on the tribrachial flame structure are still less understood.

Furthermore, diesel fuels generally have two-stage ignition processes, in which the first stage ignition is governed by low temperature chemistry and the second stage ignition dominated by high temperature chemistry. In both low and high temperature regimes, the ignition delay time decreases as the initial temperature increases. However, in the intermediate temperature regime, the transition of the ignition chemistry results in increased overall ignition delay time as the initial temperature increases. Therefore, this nonmonotonic response of the ignition delay time to increasing initial temperature is referred as the negative temperature coefficient (NTC), which has been extensively studied in homogeneous systems as a major feature of large hydrocarbon autoignition [14]. **The coupling between NTC chemistry and transport processes should be considered, for nonuniformities invariably exist in realistic combustion systems. When the transport time scale becomes comparable to that of the NTC chemical time scale, the two processes are expected to be strongly coupled. As a consequence, the global response of the inhomogeneous system can also be affected by NTC chemistry.** Recently, a series of both computational and experimental studies adopting the nonpremixed counterflow configuration by Law and co-workers [15–17] have demonstrated that, with the existence of nonuniformities in the flow, species, and temperature fields, the ignition characteristics of nonpremixed flames can be fundamentally affected by NTC effects, especially at elevated pressures and/or reduced strain rates.

Therefore, NTC-affected stabilization of nonpremixed lifted jet flames can be potentially important, yet few literatures provide detailed analysis. Krisman *et al.* [18] recently conducted a numerical study of dimethyl ether (DME)/air mixing layer at 40 atmospheres and air coflow temperatures ranging from 700 to 1500 K and observed polybrachial structures in the heat release rate profiles. The mixture fractions corresponding to the stabilization points defined based on the hydroxyl radical (OH) mass fraction and the first stage autoignition kernels based on the methoxymethylperoxy radical ($CH_3OCH_2O_2$) were compared with the most reactive mixture fractions computed from homogeneous autoignition under the same initial conditions. The transport budget analysis based on selected species was performed to differentiate deflagration from autoignition.

This previous study on the polybrachial structure is intriguing, showing the modified flame shape from autoignition

in the mixing layer. However, further investigation should be made to study the detailed chemical structure and stabilization mechanism of the polybrachial flame. For example, tools for computational diagnostics, especially for identifying locally dominant chemical reactions, are needed to understand the controlling chemistry. Moreover, a direct comparison to the homogeneous autoignition is insufficient to understand the transport processes in the current configuration. In the two-dimensional mixing layer, transport processes in two directions are important: parallel and perpendicular to the mixture fraction gradient, which are due to the transverse thermal and species concentration stratification # want to add a comma here to separate two groups and the streamwise flow evolution and flame back diffusion, respectively. These considerations would significantly improve the understanding of the role of autoignition upstream of the flame structure and quantitatively identify the controlling kinetics and stabilization mechanism.

In the present study, nonpremixed DME/air coflow flames were simulated at 30 atmospheres with the oxidizer stream heated to activate autoignition. With fixed inlet velocities, only the oxidizer stream boundary temperature was varied to investigate the corresponding lifted flame morphology, chemical structure, and dominant reaction pathways. The interaction between the autoignition front and the propagating flame and the stabilization mechanism of the lifted flame was analyzed with Chemical Explosive Mode Analysis (CEMA) and a one-dimensional Lagrangian Flamelet Analysis (LFA), which will be introduced in detail in the following sections.

2. Simulation Details

The flow configuration is an axisymmetric DME stream at 300 K in a heated coflow of air (700, 800, 900, and 1100 K) at 30 atmospheres. The fuel nozzle diameter D is 0.8 mm, and the fuel and air are initially separated with a wall with thickness $D/10$. Uniform inlet velocities of 3.2 m/s were specified for both fuel and air streams and kept the same for all the cases to obtain lifted flames.

The flow field was initialized on a coarse mesh within a large domain. At first, all the chemical source terms were set to zero until the nonreacting mixing layer reached steady-state. Chemical source term were then activated; the mixture autoignited; and the flow field reached steady-state. The domain was then truncated, and the mesh was refined to fully resolve the chemical structure. All of the results presented in this present work were obtained from steady-state solutions.

The Navier-Stokes equation with buoyancy, the conservation equations of mass, species, and energy were solved. The species diffusivities are determined from a constant, nonunity Lewis number. The Lewis numbers for individual species are pre-calculated from a one-dimensional flamelet with the same boundary conditions and the mixture-averaged transport model and evaluated at the maximum temperature location. The conserved scalar mixture fraction Z is specified as unity and zero for the fuel jet and coflow at the inlet, respectively, and computed by solving its transport equation with unity Lewis number. This definition of mixture fraction is consistent with the one used in the flamelet calculation in Sec. 4.2.

Dimethyl ether was chosen in this work, for it is a clean biofuel and one of the smallest hydrocarbon exhibiting

NTC. Detailed reaction models for low and high temperature DME oxidation [19–22] have been extensively developed and validated in burner stabilized flames [23], nonpremixed counterflow flame ignition [24], and laminar flame speeds [25]. The present computations were conducted using a skeletal mechanism of 39 species [26], including both low and high temperature oxidation pathways, which was reduced from the well validated detailed mechanism of Zhao *et al.* [22].

The low-Mach number formulation of the governing equations is solved using NGA, which is based on the numerical methods of Desjardins *et al.* [27]. The momentum and scalar equations are discretized with a second-order centered scheme and a third-order WENO scheme [28], respectively, on a staggered mesh. The iterative second-order semi-implicit Crank-Nicolson scheme of Pierce and Moin [29] is adopted for temporal integration. At each time step, the chemical source terms for species and energy equations are evaluated independently from the transport terms using the CVODE package [30].

Uniform grids in the axis direction were adopted for the computations, and the grid spacing was set as $\Delta x = 2.2$ microns. A nonuniform grid was used in the radial direction with a minimum grid spacing of 2.5 microns and stretching rate of less than 3%. The computational domain dimensions and number of grid points for each simulation are summarized in Table 1.

A grid convergence was performed for the air temperature 800 K case, as it has the most complex structure, which is discussed in the following sections. As shown in Fig. 1, grid convergence was achieved for velocity, temperature, and species profiles. Grid convergence was also verified for the air temperature 1100 K case, which shows similar results and is therefore not shown here.

3. Thermal and Chemical Structure

To visualize the flame structures, the heat release rates profiles for the four cases (700, 800, 900, and 1100 K) are shown in Fig. 2. Qualitatively, the most upstream point on the largest heat release contour, colored by red, was estimated as the stabilization point.

At 700 K, a tribrachial thermal structure is observed, and the stabilization point locates around $Z = 0.15$, which is richer than the triple point, where the three branches intersect. Moreover, compared to the classical triple flame structure, the middle heat release rate branch, corresponding to the nonpremixed flame, is significantly weaker than the other two branches.

At 800 K, the stabilization point does not locate on the triple flame structure any more. Instead, it locates near $Z = 0.23$ and connects two trailing heat release branches, where a tribrachial flame structure attaches to the leaner branch **(LB) of the bibrachial reacting front**. A schematic of the structure is shown in Fig. 3.

As the air boundary temperature increases to 900 K, the stabilization point shifts back to $Z = 0.14$. Moreover, a long trailing branch at richer mixture fraction is attached to main triple flame, resulting in a tetrabrachial structure. Compared with the structure shown in the 800 K case, the main triple flame stabilizes further upstream, as it depends

less on the radical accumulation ahead of the flame. Therefore, it catches up with the reacting front at richer mixture fraction, and they merge as the tetrabrachial structure.

A further increase in the boundary temperature results in a structure that is very similar to the classical triple flame, except for the fact that there is also heat release ahead of the stabilization point at $Z = 0.13$. Some of the multibrachial structures were also observed by Krisman *et al.* [18], using different definitions for branches, and it was concluded in that reference that the autoignition chemistry could affect the flame structure and the stabilization mechanism. # They defined branches differently.

To first qualitatively demonstrate the chemical structure of the flame, selected species profiles were examined, shown in Figures 4 to 7. The methoxymethylperoxy radical ($\text{CH}_3\text{OCH}_2\text{O}_2$) and hydroxyl radical (OH) were chosen as indicators of low and high temperature chemistry, respectively. The hydroperoxyl radical (HO_2) and hydrogen peroxide (H_2O_2) were chosen, for they form in the preheat zone of a flame or before autoignition but quickly vanish in the post flame zone or after ignition [31].

For all four cases, similar profiles can be seen for some species. First, the low temperature chemistry, which is indicated by the $\text{CH}_3\text{OCH}_2\text{O}_2$ radical, is found to be important at richer mixture fractions, where the temperature is lower. Second, the OH radical peaks in the flame region and correlates well with the triple flame structure shown in the heat release rate profiles. Third, HO_2 mass fraction peaks in a thin region. Compared with the heat release rate contours, this thin region outlines the flame front and the reactive mixture at the rich mixture fractions and indicates the importance of the exothermic three-body recombination reaction $\text{H} + \text{O}_2 + \text{M} \rightleftharpoons \text{HO}_2 + \text{M}$.

However, there are also differences in the chemical structure among cases. For example, for the 800 and 900 K cases, another OH local maxima, which is two orders of magnitudes smaller than the peak value on the triple flame, appears at richer mixture fractions, right downstream of where the $\text{CH}_3\text{OCH}_2\text{O}_2$ radical and H_2O_2 disappear, indicating autoignition. Moreover, more pronounced differences between the three lower boundary temperature cases and the 1100 K case are shown in the H_2O_2 profiles: for the lower boundary temperature cases, H_2O_2 accumulates along mixture fraction iso-contours until it decomposes at the flame region, while for the 1100 K case, H_2O_2 accumulation is an order of magnitude lower, due to the reduced residence time from the nozzle exit to the flame base. # I first talked about the thermal structure and determined multibrachial structure accordingly. Species profiles were analyzed to show the chemical structure. This has been pointed out at the very beginning of the species profile discussion. Moreover, the section title implies that we are going to talk about both thermal and chemical structures.

4. Computational Diagnostics

4.1. Chemical Explosive Mode Analysis

Besides the analysis based on selected species profiles, Chemical Explosive Mode Analysis (CEMA) was conducted. CEMA was developed by Lu and co-workers [32, 33] to identify the controlling chemistry in complex reacting flows. Briefly, the eigenvalues of the Jacobian matrix of the chemical source term based on the local species

concentrations and temperature are evaluated and determined as the chemical modes. The largest positive eigenvalue, which is defined as the chemical explosive mode, describes the rate of system runaway. The projection of a reaction on the explosive mode is defined as the explosion participation index to account for its contribution to the explosive mode.

Specifically, in the present study, the dominant reactions at representative locations, such as those upstream and near the flame base are identified, based on the explosive mode and participation index. For each case, the local species concentrations and temperature were sampled along the Z_{st} , $Z = 0.2$, and $Z = 0.3$ iso-contours and processed by CEMA to demonstrate the evolution of the dominant reactions.

The CEMA results are summarized in Fig. 8, where three representative locations along the Z_{st} iso-contour approaching the flame front and two locations ahead of and at the reaction front at $Z = 0.2$ were sampled. For the three lower coflow temperature cases, similar chemical patterns were found. Upstream of the flame front, the eigenvalues of the chemical modes are positive, indicating that the mixtures have the potential to explode; after the flame front, the eigenvalues become negative, meaning that the mixtures are composed of burned products. Following the Z_{st} iso-contour, the hydrogen peroxide chain branching reaction ($H_2O_2 + M \rightleftharpoons OH + OH + M$) is the reaction that has the largest projection on the explosive mode, showing the dominant role of autoignition chain branching. The characteristic DME low temperature chemistry is also important upstream of the flame, where methoxymethylperoxy radical formation ($CH_3OCH_2 + O_2 \rightleftharpoons CH_3OCH_2O_2$) and isomerization ($CH_3OCH_2O_2 \rightleftharpoons CH_2OCH_2O_2H$) promote the explosion, while the β -scission reaction ($CH_2OCH_2O_2H \rightleftharpoons OH + CH_2O + CH_2O$) retards the explosion. Approaching the flame front, the H radical recombination reaction ($H + O_2 + M \rightleftharpoons HO_2 + M$) becomes important for the 700 – 900 K cases, due to the fact that the H radicals generated at the reaction zone diffuse upstream and undergo three-body recombination reactions under the high pressure, low temperature condition. Further downstream where the heat release rate peaks, the hydrogen branching reaction ($H + O_2 \rightleftharpoons O + OH$) becomes the most important chain branching reaction, indicating that the combustion mode shifts from autoignition to flame propagation. The nature of the tribrachial structure (around Z_{st}) at 700 – 900 K is therefore identified: an autoignition assisted premixed flame front.

CEMA conducted along the $Z = 0.2$ iso-contour, which crosses the rich heat release front in the 800 and 900 K cases, shows different chemical mode evolution. The H_2O_2 chain branching reaction is always the dominant reaction that promotes the explosive mode, while the H radical recombination reaction and the H branching reaction is less important ahead of the rich heat release front and at the front. Therefore, this heat release front is dominated by autoignition chemistry rather than flame chemistry and is characterized as an autoignition front.

On the contrary, although low temperature chemistry is still important for the 1100 K case upstream of the reaction zone and the hydrogen chain branching reaction promotes explosion at the reaction zone, the hydrogen peroxide chain branching reaction is not very important for all the sampled locations. Since the hydrogen peroxide reaction is the crucial chain branching reaction for the autoignition process, it is concluded that the 1100 K case is less affected by autoignition chemistry than the lower boundary temperature cases.

4.2. Lagrangian Flamelet Analysis

The above species profile analysis and CEMA results have demonstrated that autoignition chemistry is crucial to the complex flame structure in the 700 to 900 K cases. However, the role that autoignition plays in the stabilization still needs further investigation. To elucidate the role of autoignition for the current flow configuration, a direct comparison with the homogeneous counterpart for a Lagrangian flow particle is insufficient, for the transport effects both parallel and perpendicular to the mixture fraction gradient are neglected. First, the temperature and species stratification along mixture fraction gradient can significantly modify the ignition characteristics, especially for fuels with NTC chemistry [15, 17]. Second, flame propagation perpendicular to the mixture fraction gradient can also influence the autoignition front through thermal and radical back diffusion.

The unsteady flamelet analysis was conducted to account for diffusion parallel to mixture fraction gradients, and comparisons with two-dimensional CFD simulation can then demonstrate the dominant stabilization mechanism. If the thermal structure is stabilized by (nonpremixed) autoignition, following the mixture fraction iso-contour, the spatial information from the two-dimensional simulation could be interpreted as the time history of the corresponding mixture and predicted by the evolution of the flamelet. Conversely, if premixed flame propagation is the dominant stabilization mechanism, the flamelet solution would not agree well with the CFD simulation, since the transport processes along the mixture fraction iso-contour is not negligible compared to the gradient direction.

The unsteady flamelet model developed by Pitsch *et al.* [34], which is called the Lagrangian Flamelet Analysis (LFA), was adopted to investigate the evolution of the autoignitive mixing layer. Due to mixing processes, the scalar dissipation rate χ , which can influence the flamelet solution significantly, decreases in the streamwise direction. Therefore, this dissipation rate variation should be considered when simulating a flamelet as it evolves downstream.

In the present study, the unsteady flamelet was simulated with FlameMaster [35], and the dissipation rate was specified as a function of the flamelet time. The flamelet time was computed from the NGA simulation results, along the stoichiometric mixture fraction Z_{st} iso-contour:

$$t = \int_0^x \frac{1}{(u + u_Z)(x')(Z = Z_{st})} dx'. \quad (1)$$

This formulation is otherwise the same as in Pitsch *et al.* [34], except that, in addition to the axial component of the fluid convection velocity u , the axial component of the mixture fraction iso-contour propagation speed relative to the fluid convection u_Z is also taken into account. The expression for the constant property scalar iso-surface velocity relative to the local fluid motion was derived by Pope [36], and the current work adopts the formulation derived by Lignell *et al.* [37] for variable properties:

$$\mathbf{u}_Z = -\frac{\nabla \cdot (\rho D_Z \nabla Z)}{\rho |\nabla Z|} \mathbf{n}, \quad (2)$$

where D_Z is the mixture fraction diffusivity and ρ is the density. The normal vector \mathbf{n} , defined as

$$\mathbf{n} = \frac{\nabla Z}{|\nabla Z|}, \quad (3)$$

indicates the direction of this diffusion induced relative velocity. The dissipation rate along the $Z_{st} = 0.1005$ iso-contour obtained from the NGA simulation was then correlated with this flamelet time and provided as the input for the FlameMaster calculation. The dissipation rates at other mixture fractions were computed assuming the following form [38]:

$$\chi(Z) = \chi(Z_{st}) \frac{\exp(-2[\text{erfc}^{-1}(2Z)]^2)}{\exp(-2[\text{erfc}^{-1}(2Z_{st})]^2)} = \chi(Z_{st})f(Z; Z_{st}). \quad (4)$$

To validate this formulation in the current configuration, the dissipation rates along different mixture fraction iso-contours were sampled from the NGA simulation, normalized using Eq. 4, and compared with the sampling along the Z_{st} iso-contour. As shown in Fig. 9, the normalized dissipation rates at different mixture fractions all collapse to the value at Z_{st} . Therefore, only the dissipation rate samplings along the Z_{st} iso-contour were needed to perform the unsteady flamelet calculation.

To account for the differential diffusion, species Lewis numbers for LFA were specified the same as in the NGA simulation. The governing equations for species and temperature follow Eq. 24 and 25 in Pitsch and Peters [39].

In the current work, the time history of the dissipation rate χ_{st} was specified in FlameMaster according to the NGA simulation. To avoid the ill-defined Lagrangian time in the recirculation zone, time zero was defined at a downstream location ten times the thickness of the wall. Accordingly, the species and temperature profiles along the radial cut at this location were specified as the initial conditions for the flamelet. Based on these initial conditions and χ_{st} time history profiles, the unsteady flamelets were calculated and compared with the two-dimensional simulation results for Z_{st} , $Z = 0.2$, and $Z = 0.3$.

As shown in Fig. 10, two ignition stages can be seen at Z_{st} and $Z = 0.2$ for the 700 K case, while at $Z = 0.3$ only one ignition dominated by low temperature chemistry is observed, due to the reduced initial temperature. For the 800 K case, both the flamelet and two-dimensional simulation experience almost identical time histories, where two-stage ignition happens at all three mixture fractions. As the initial temperatures further increase, corresponding to the increase in the boundary temperatures in the CFD simulation, the two-stage ignition phenomenon is less pronounced. However, the 900 K case still shows good agreement between the flamelet profile with the time history of the two-dimensional simulation, similar to the above two cases.

On the contrary, for the 1100 K case, the ignition delay time computed with the one-dimensional flamelet assumption is significantly longer than the two-dimensional counterpart, indicating that autoignition is less important to the stabilization mechanism and the transport processes along the mixture fraction iso-contours must be important. Noting that the scalar dissipation rate other than χ_{st} is modeled through Eq. 4, small differences between the flamelet and CFD results are expected, even for an autoignition dominated case. However, compared with the above three cases, the significant ignition delay at 1100 K suggests that flame propagation dominates the stabilization of the flame structure.

5. Stabilization Mechanism

With the above analysis based on species profiles, Chemical Explosive Mode Analysis, and Lagrangian Flamelet Analysis, the transition of the stabilization mechanism and the coupling between autoignition chemistry and flame propagation can be clearly identified. In the current study, two fundamental stabilization mechanisms are relevant: the *kinetic* stabilization mechanism, due to the balance between the autoignition delay time and flow residence time, and the *kinematic* stabilization mechanism, due to the balance between the premixed flame propagation velocity and the local flow velocity.

In this stratified composition and temperature field, autoignition and flame propagation processes are coupled through thermal and radical interactions, for the accumulation of the upstream radicals and heat release from autoignition accelerate the flame propagation velocity. The flame also transfers heat and radicals through back diffusion processes to the upstream, which could also facilitate autoignition.

For the current study, a purely *kinetically* stabilized autoignition front was not observed, for the classical triple flame structures are seen at certain locations, and the flame chemistry is dominant at the flame front. However, as demonstrated above, the *kinetic* stabilization is the dominant mechanism for the 700 to 900 K cases, for the steady flame structure is assisted and stabilized by autoignition. Specifically, as seen from Fig. 2, the nonpremixed branch of the tribrachial flame structure has quite low heat release rate for the 700 K case, suggesting relatively weaker flame chemistry compared to autoignition. As the boundary temperature increases to 800 K, an autoignition front stabilizes the multibrachial structure at rich mixture fractions, due to shorter ignition delay time resulting from the NTC chemistry, and a modified triple flame structure stabilizes slightly downstream of this front at leaner mixture fractions. Further increasing boundary temperature results in higher flame propagation velocity; therefore, the flame front at leaner mixture fraction depends less on the radicals accumulation ahead of the flame and propagates upstream, although the overall structure is still stabilized *kinetically*. The transition to a *kinematically* stabilized flame structure is achieved for the 1100 K case, where the flame propagation velocity balances the local incoming flow velocity; therefore, the flame structure stabilizes close to the nozzle exit and depends least on the radical accumulation from upstream.

Based on the understanding obtained from the current study, further extension of the stabilization regime can be made, as shown in Fig. 11. For fixed inlet flow velocity, when the boundary temperature is sufficiently low, the mixture cannot be autoignited, and it is essentially frozen flow. Even when an external ignition source is applied, the flame cannot keep up with the excessive high flow velocity, such that the flame blows off. When the boundary temperature is high enough to activate autoignition, autoignition happens far downstream, but the flame propagation velocity still cannot keep up with the flow velocity. As a consequence, a pure *kinetically* stabilized autoignition front can be achieved. Due to the computational cost required for such a large domain, the purely *kinetically* stabilized case was not simulated. Conversely, when the boundary temperature is sufficiently high, the flame stabilizes close to the inlet, where the upstream can be treated as frozen flow, due to reduced residence time, which is similar to the

1100 K case. Therefore, a purely *kinematically* stabilized classical triple flame structure is achieved. Further increase in the boundary temperature results in an attached flame with the increased flame speed. Although not included in the current paper, an attached flame was simulated at 1500 K. In between the purely *kinetically* and *kinematically* stabilized regimes, there is a transitional regime governed by both mechanisms, which corresponds to the 700 to 900 K cases. Due to the NTC behavior of the autoignition chemistry, the stabilization point, in terms of mixture fraction space, varies, and the complex multibrachial flame structure appears.

6. Conclusions

In the present study, two-dimensional nonpremixed DME flames in heated air coflows were simulated. The simulation was conducted at 30 atmospheres to observe the influence of NTC chemistry on the stabilization mechanism. A uniform and fixed inlet boundary velocity was specified, and four coflow temperature (700, 800, 900, and 1100 K) cases were studied. **The heat release rate profiles and characteristic species profiles for low and high temperature autoignition and premixed flame propagation were examined.**

The heat release rate profile, characteristic species profiles for low and high temperature chemistry, autoignition, and premixed flame propagation were examined. Further investigation based on Chemical Explosive Mode Analysis and Lagrangian Flamelet Analysis enabled the determination of the stabilization mechanism.

The 700 to 900 K cases were characterized as *kinetically* stabilized, due to the dominant role of autoignition chemistry. As the boundary temperature increases, the leading point of the heat release profile shifts to richer mixture fractions and then shifts back, due to the NTC effect on the autoignition process and the coupling between the autoignition and premixed flame propagation chemistry.

The 1100 K case was characterized as *kinematically* stabilized, for it exhibits the classical triple flame structure, with stabilization achieved due to the balance between the premixed flame propagation velocity and the local incoming flow velocity.

Based on the current simulation results, extended stabilization regimes were identified. For sufficiently high inlet velocity, as the boundary temperature increases from the cold case, frozen flow is first achieved, where the mixture is nonautoignitive, and even the flame generated by external ignition source will blow off. When the mixture can be autoignited, the *kinetically* stabilized autoignition front gradually transits to a *kinematically* stabilized classical triple flame, where the premixed flame front propagation velocity balances the local incoming flow velocity. The triple flame will eventually become attached when the boundary temperature is sufficiently high, and the flame speed is sufficiently fast.

Further study on the effects of fuel dilution and inlet velocity on the lift-off height, stabilized flame structure, and stabilization mechanism, is suggested. For example, boundary velocity can be varied to change the flow residence time, and dilution can be added to the fuel stream to change the chemical time scale. Moreover, if autoignition is the dominant stabilization mechanism and the scalar dissipation rate sufficiently low, the nonmonotonic lifted height vari-

ation can be observed as the boundary temperature changes, which is a plausible prediction based on the homogeneous autoignition and nonpremixed counterflow observation [17].

References

- [1] J. Buckmaster, *Prog. Energy Combust. Sci.* 28 (2002) 435–475.
- [2] S. H. Chung, *Proc. Combust. Inst.* 31 (2007) 877–892.
- [3] J. W. Dold, *Combust. Flame* 76 (1989) 71–88.
- [4] L. J. Hartley, J. W. Dold, *Combust. Sci. Technol.* 80 (1991) 23–46.
- [5] S. Ghosal, L. Vervisch, *J. Fluid Mech.* 415 (2000) 227–260.
- [6] M. K. Kim, S. H. Won, S. H. Chung, *Proc. Combust. Inst.* 31 (2007) 901–908.
- [7] G. R. Ruetsch, L. Vervisch, A. Liñán, *Phys. Fluids* 7 (1995) 1447.
- [8] B. J. Lee, S. H. Chung, *Combust. Flame* 109 (1997) 163–172.
- [9] T. Plessing, P. Terhoeven, N. Peters, M. S. Mansour, *Combust. Flame* 115 (1998) 335–353.
- [10] P. N. Kioni, K. N. C. Bray, D. A. Greenhalgh, B. Rogg, *Combust. Flame* 116 (1999) 192–206.
- [11] B. C. Choi, K. N. Kim, S. H. Chung, *Combust. Flame* 156 (2009) 396–404.
- [12] B. C. Choi, S. H. Chung, *Combust. Flame* 157 (2010) 2348–2356.
- [13] B. C. Choi, S. H. Chung, *Combust. Flame* 159 (2012) 1481–1488.
- [14] J. Zádor, C. A. Taatjes, R. X. Fernandes, *Prog. Energy Combust. Sci.* 37 (2011) 371–421.
- [15] C. K. Law, P. Zhao, *Combust. Flame* 159 (2012) 1044–1054.
- [16] P. Zhao, C. K. Law, *Combust. Flame* 160 (2013) 2352–2358.
- [17] S. Deng, P. Zhao, D. Zhu, C. K. Law, *Combust. Flame* 161 (2014) 1993–1997.
- [18] A. Krisman, E. R. Hawkes, M. Talei, A. Bhagatwala, J. H. Chen, *Proc. Combust. Inst.* (2014).
- [19] H. J. Curran, W. J. Pitz, C. K. Westbrook, P. Dagaut, J.-C. Boettner, M. Cathonnet, *Int. J. Chem. Kinet.* 30 (1998) 229–241.
- [20] S. L. Fischer, F. L. Dryer, H. J. Curran, *Int. J. Chem. Kinet.* 32 (2000) 713–740.
- [21] H. J. Curran, S. L. Fischer, F. L. Dryer, *Int. J. Chem. Kinet.* 32 (2000) 741–759.
- [22] Z. Zhao, M. Chaos, A. Kazakov, F. L. Dryer, *Int. J. Chem. Kinet.* 40 (2008) 1–18.
- [23] E. W. Kaiser, T. J. Wallington, M. D. Hurley, J. Platz, H. J. Curran, W. J. Pitz, C. K. Westbrook, T. J. Wallington, *J. Phys. Chem. A* 104 (2000) 8194–8206.
- [24] X. L. Zheng, T. F. Lu, C. K. Law, C. K. Westbrook, H. J. Curran, T. Berces, F. L. Dryer, *Proc. Combust. Inst.* 30 (2005) 1101–1109.
- [25] X. Qin, Y. Ju, *Proc. Combust. Inst.* 30 (2005) 233–240.
- [26] G. Bansal, J. H. Chen, T. F. Lu, Z. Luo, in: 13th Int. Conf. Numer. Combust., Corfu, Greece.
- [27] O. Desjardins, G. Blanquart, G. Balarac, H. Pitsch, *J. Comput. Phys.* 227 (2008) 7125–7159.
- [28] X. Liu, S. Osher, T. Chan, *J. Comput. Phys.* 115 (1994) 200–212.
- [29] C. D. Pierce, P. Moin, *Progress-variable Approach for Large-Eddy Simulation of Turbulent Combustion*, Ph.D. thesis, Stanford University, 2001.
- [30] S. D. Cohen, A. C. Hindmarsh, P. F. Dubois, *Comput. Phys.* 10 (1996) 138.
- [31] C. S. Yoo, R. Sankaran, J. H. Chen, *J. Fluid Mech.* 640 (2009) 453–481.
- [32] T. F. Lu, C. S. Yoo, J. H. Chen, C. K. Law, *J. Fluid Mech.* 652 (2010) 45–64.
- [33] R. Shan, C. S. Yoo, J. H. Chen, T. Lu, *Combust. Flame* 159 (2012) 3119–3127.
- [34] H. Pitsch, M. Chen, N. Peters, *Symp. Combust.* 27 (1998) 1057–1064.
- [35] H. Pitsch, *FlameMaster*, A C++ computer program for 0D combustion and 1D laminar flame calculations.
- [36] S. B. Pope, *Int. J. Eng. Sci.* 26 (1988) 445–469.

- [37] D. O. Lignell, J. H. Chen, P. J. Smith, T. Lu, C. K. Law, *Combust. Flame* 151 (2007) 2–28.
- [38] N. Peters, *Turbulent Combustion*, Cambridge University Press, 2000.
- [39] H. Pitsch, N. Peters, *Combust. Flame* 114 (1998) 26–40.

List of Figures

1	Velocity, temperature, and H_2O_2 profiles along Z_{st} on the nominal and two times coarser (in each direction) meshes for an air temperature of 800 K.	14
2	Heat release rate [$\text{J}/\text{m}^3\text{-s}$] profiles. The iso-contours of Z_{st} , $Z = 0.2$, and $Z = 0.3$ are outlined from right to left in solid lines, respectively. The CEMA sampling points at 800 and 1100 K are marked along the iso-contours.	15
3	A schematic of the thermal structure of the 800 K case. LPF, RPF, and NPF denotes the lean premixed, rich premixed, and nonpremixed flame branch on the triple flame structure, respectively. LB and RB denotes the leaner and richer branch of the reacting front, respectively.	16
4	Hydroxyl radical mass fraction profiles. The mixture fraction iso-contours are the same as in Fig. 2. .	17
5	Methoxymethylperoxy radical mass fraction profiles. The mixture fraction iso-contours are the same as in Fig. 2.	18
6	Hydroperoxyl radical mass fraction profiles. The mixture fraction iso-contours are the same as in Fig. 2.	19
7	Hydrogen peroxide mass fraction profiles. The mixture fraction iso-contours are the same as in Fig. 2.	20
8	Normalized participation index at 800 K and 1100 K. Sampled locations are marked in Fig. 2.	21
9	$\frac{\chi(Z)}{f(Z, Z_{\text{st}})}$, using Eq. 4, based on NGA simulation at 800 K.	22
10	Comparison between NGA and LFA results.	23
11	Regime diagram of the stabilization mechanism as coflow boundary temperature increases.	24

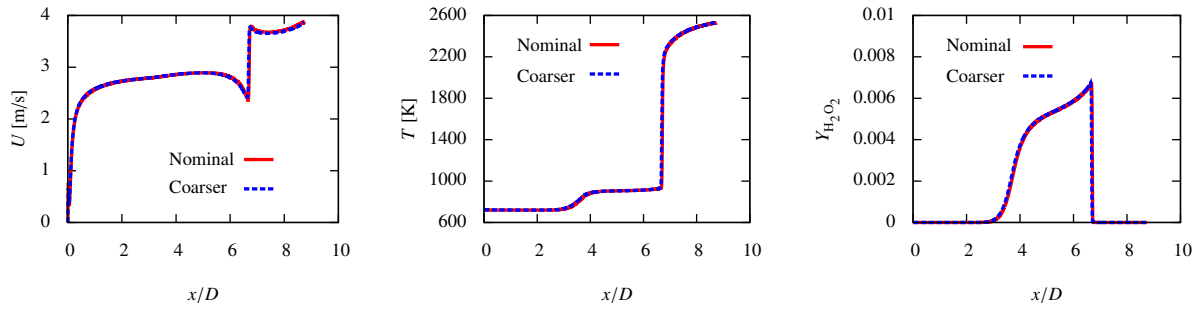


Figure 1: Velocity, temperature, and H_2O_2 profiles along Z_{st} on the nominal and two times coarser (in each direction) meshes for an air temperature of 800 K.

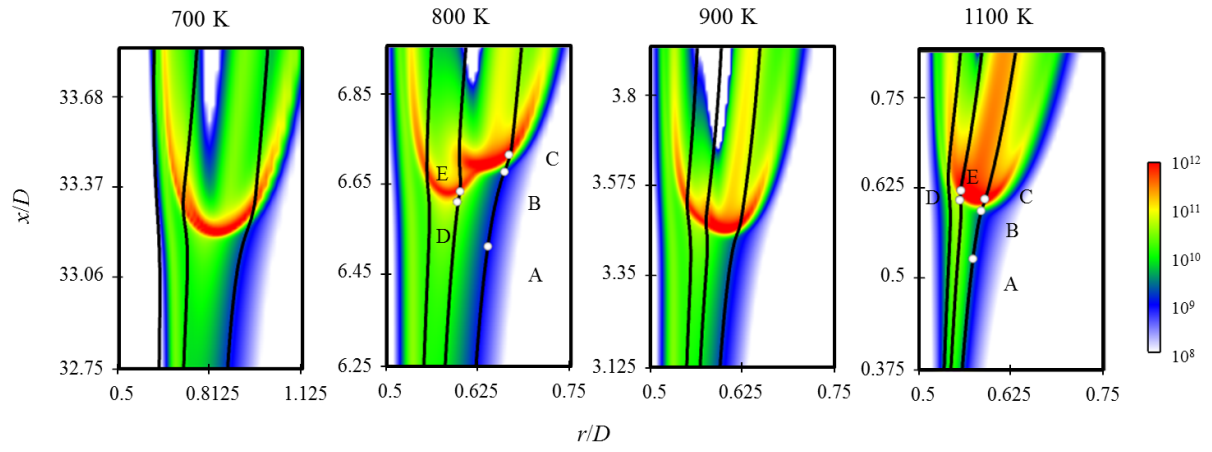


Figure 2: Heat release rate [$\text{J/m}^3\text{-s}$] profiles. The iso-contours of Z_{st} , $Z = 0.2$, and $Z = 0.3$ are outlined from right to left in solid lines, respectively. The CEMA sampling points at 800 and 1100 K are marked along the iso-contours.

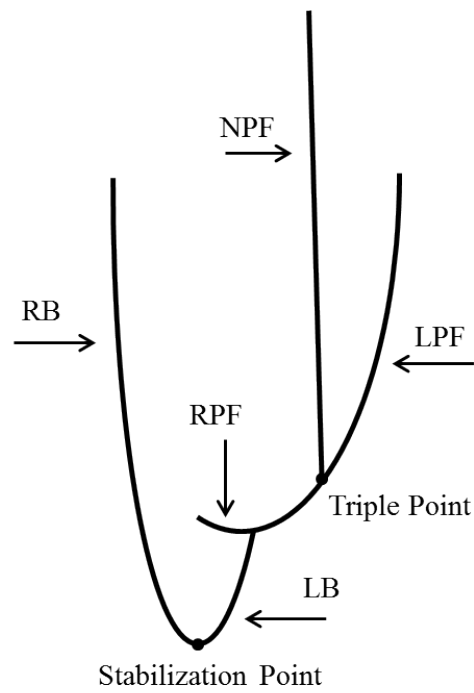


Figure 3: A schematic of the thermal structure of the 800 K case. LPF, RPF, and NPF denotes the lean premixed, rich premixed, and nonpremixed flame branch on the triple flame structure, respectively. LB and RB denotes the leaner and richer branch of the reacting front, respectively.

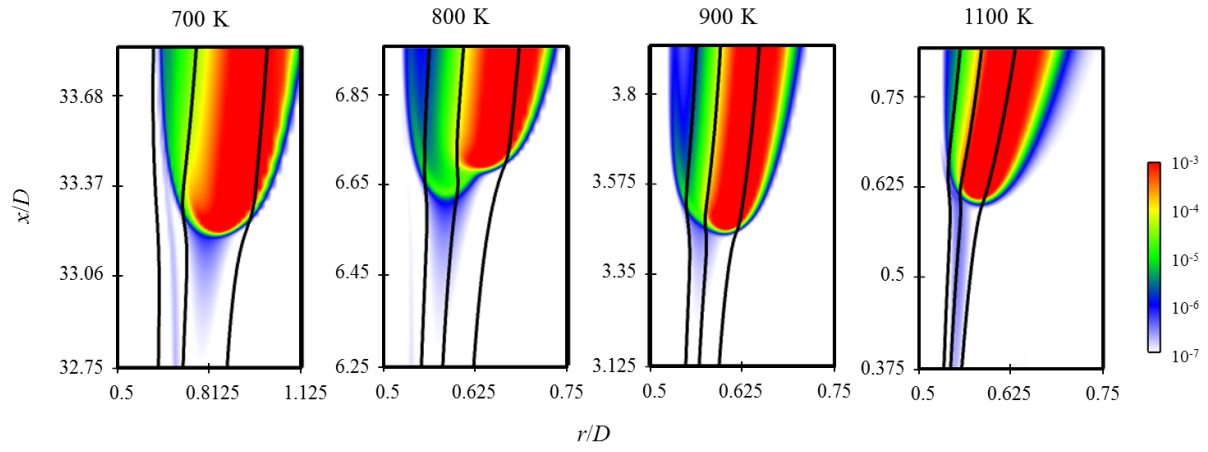


Figure 4: Hydroxyl radical mass fraction profiles. The mixture fraction iso-contours are the same as in Fig. 2.

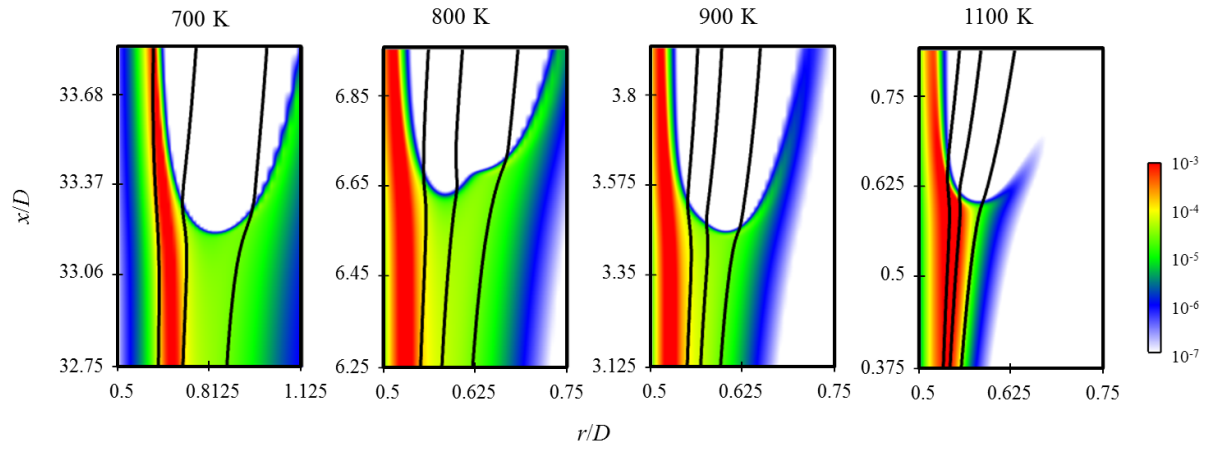


Figure 5: Methoxymethylperoxy radical mass fraction profiles. The mixture fraction iso-contours are the same as in Fig. 2.

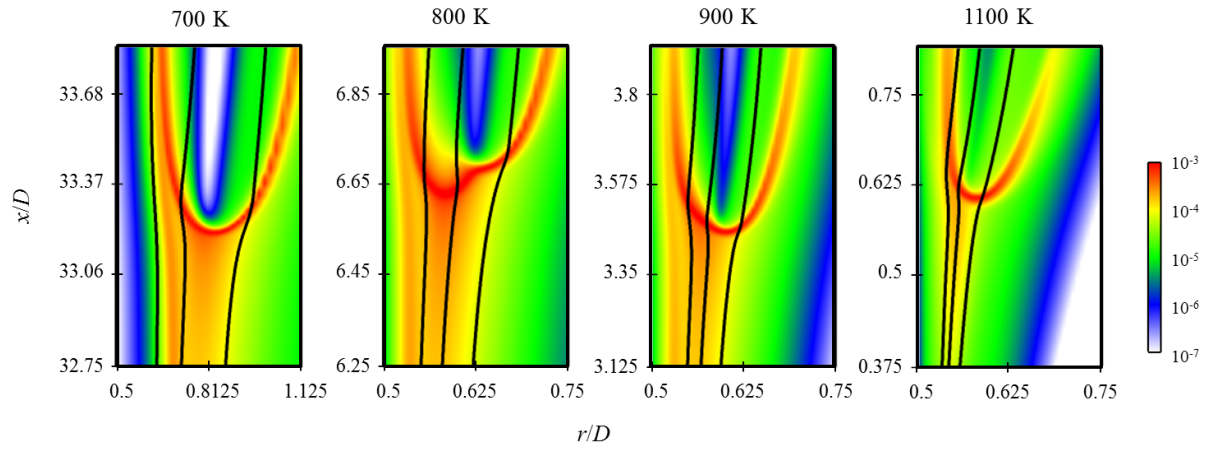


Figure 6: Hydroperoxyl radical mass fraction profiles. The mixture fraction iso-contours are the same as in Fig. 2.

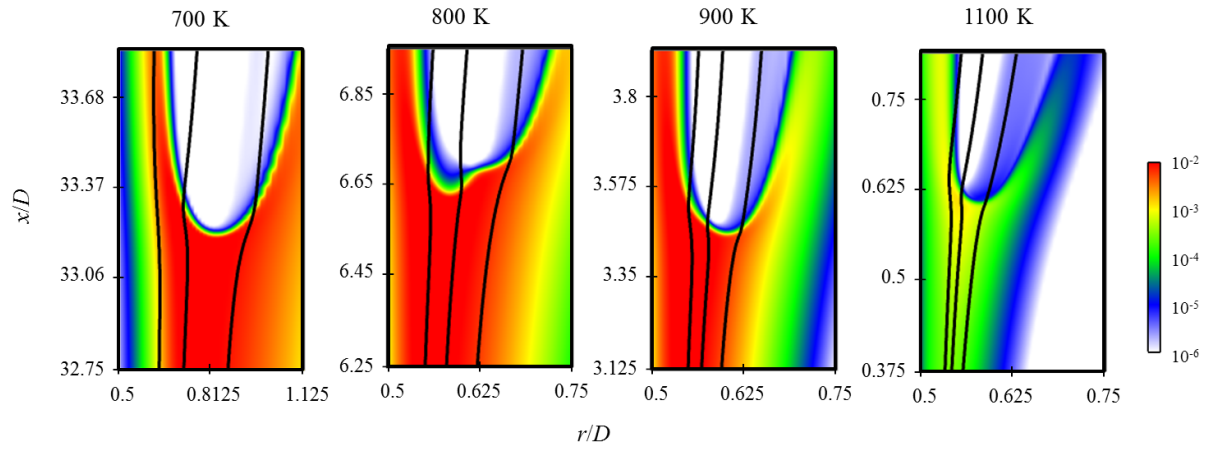


Figure 7: Hydrogen peroxide mass fraction profiles. The mixture fraction iso-contours are the same as in Fig. 2.

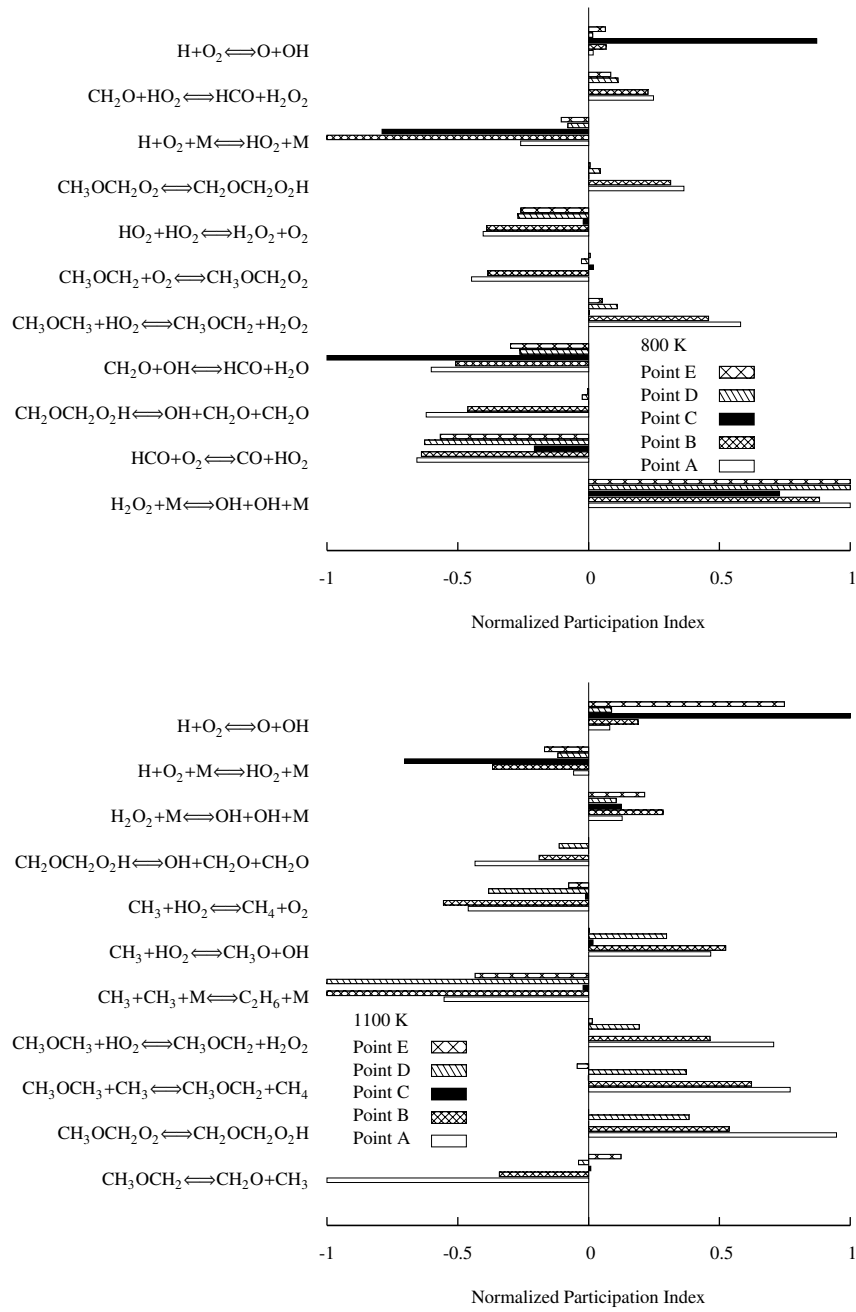


Figure 8: Normalized participation index at 800 K and 1100 K. Sampled locations are marked in Fig. 2.

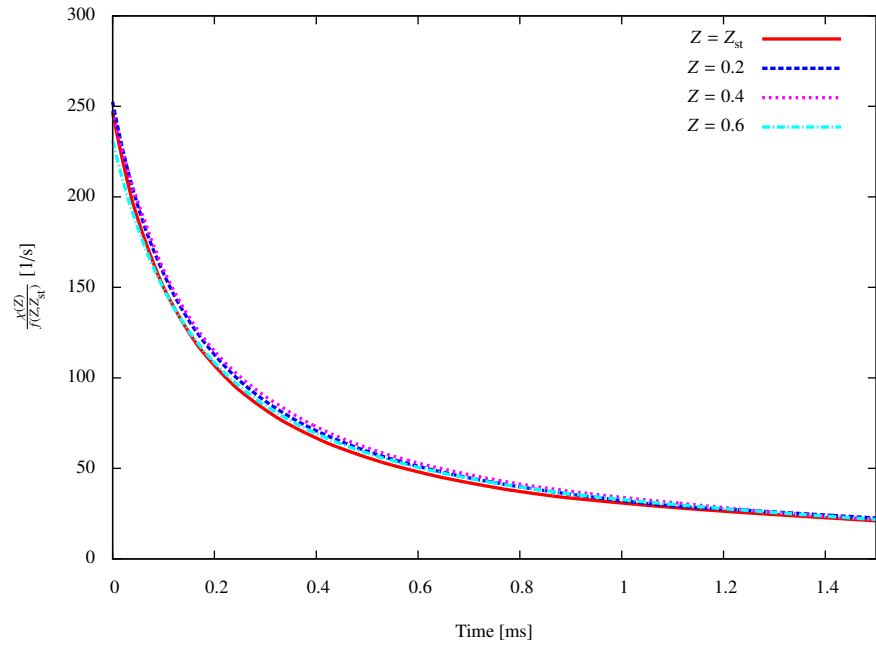


Figure 9: $\frac{\chi(Z)}{f(Z, Z_{st})}$, using Eq. 4, based on NGA simulation at 800 K.

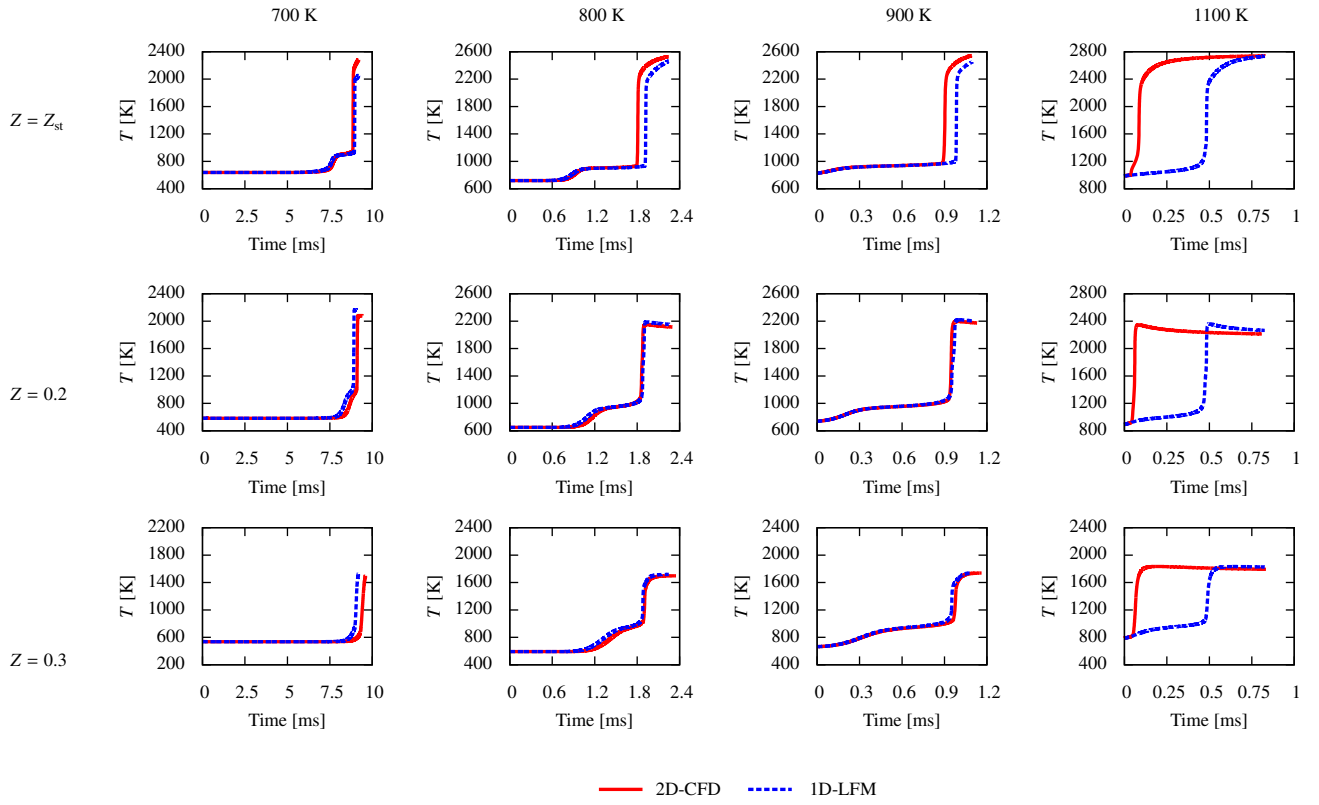


Figure 10: Comparison between NGA and LFA results.

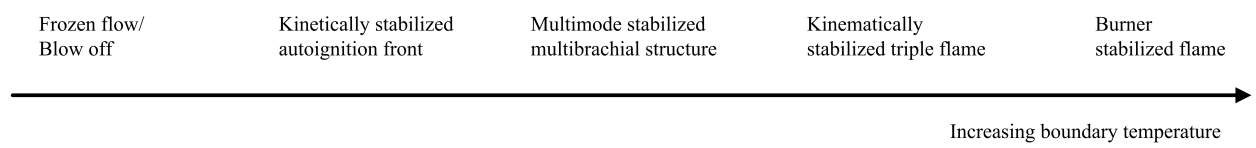


Figure 11: Regime diagram of the stabilization mechanism as coflow boundary temperature increases.

List of Tables

1	Computational domain and number of grid points.	26
---	---	----

Table 1: Computational domain and number of grid points.

Coflow Temperature [K]	700	800	900	1100
Length [mm]	28	7	3.5	3
N_x	12290	3072	1536	1282
N_r	192	176	176	192